

Comparison of three different strategies to introduce anisotropic interface properties in a multi-phase-field model

Martin Minar and Nele Moelans*
KU Leuven, Department of Materials Engineering
(Dated: January 5, 2022)

Three different strategies of model parameters determination in an established multi-phase field model were quantitatively compared with emphasis on inclination-dependent interface energy and kinetic coefficient. Both the match to Wulff shape and its shrinkage rates were quantified. Also, the three model modifications were quantitatively compared in the results of triple junction angles, to confirm that only one of the three was thermodynamically consistent for strong anisotropies. Additionally, the combined effect of inclination dependence in GBE and in GB mobility was studied. All simulations were performed over wide intervals of physical cases and various numerical settings at the interface to provide thorough validation of the model.

I. INTRODUCTION

Even though grain boundary energy (GBE) in pure polycrystalline metals is known to be inclination-dependent [1–3], multi phase field simulations of grain growth most often assume either isotropic grain boundary properties [4–8], Read-Shockley misorientation dependence of GBE [9] or other physics affecting the polycrystalline microstructure evolution such as diffusion or multiple phases [10–13]. The inclination-dependent GBE was included in several studies [14–18], however its validation was usually carried out by qualitative comparison to corresponding Wulff shape without quantifying the accuracy of match or its dependence on strength of anisotropy or finite interface width. The multi-phase field model by Moelans [19] is an established [20] quantitative phase field model of grain growth with anisotropic grain boundary properties. Also, it was extended to include multicomponent diffusion [21], which allowed simulations of diffusive phase transformations.

Using asymptotic analysis, Moelans derived that in the original model [19], the local interface energy and width are related to three model parameters. Because these are two equations of three variables, the system is undetermined and one of the model parameters is free. This degree of freedom introduces the possibility of many different parameters assignment strategies, all of which are equivalent. Moelans proposed one, which assured constant interface width irrespective of the strength of anisotropy in interface energy. However, this approach (here denoted IWc) does not reproduce well the angles between interfaces in triple junctions for stronger anisotropies. This was already first noted by Moelans in [22]. An alternative parameters assignment strategy with variable interface width (here denoted IWvG) was used in [11, 20], but no systematic comparison was made. Additionally, the inclination dependence of interface energy in IWvG has not yet been addressed.

For this reason, a thorough comparison of IWc and

IWvG model modifications was carried out in this paper in 2D simulations. Moreover, a third parameters determination strategy (IWvK) is proposed here and compared with the former two as well.

This paper is organized as follows: firstly, the base model and its three variants are introduced, including the inclination dependence in interface energy. With inclination-dependent interface energy, the governing equations are different in each variant due to the model formulation. Secondly, the difference in the shapes of the phase field profiles in the interface for the model modifications is demonstrated in simulation with two shrinking circles. Additionally, their shrinkage rate is compared to an analytic model. Then, triple junction angles are determined. Next follows a quantitative validation of the match of phase field contour to Wulff shape in simulations with inclination-dependent interface energy. The Wulff shape shrinkage rate was analytically derived to validate the kinetics of the model. Lastly, the combined effect of the inclination dependence in kinetic coefficient and the interface energy is studied. For all simulations the effect of interface width and number of grid points through interface are investigated by re-running the simulations at different numerical settings.

II. MODEL

The system consists of n non-conserved continuous-field variables (further denoted phase fields) $\eta_1(\mathbf{r}, t), \eta_2(\mathbf{r}, t), \dots, \eta_n(\mathbf{r}, t)$, which are functions of space and time. The total free energy of the system is expressed as functional of the phase fields and their gradients $\nabla\eta_1(\mathbf{r}, t), \nabla\eta_2(\mathbf{r}, t), \dots, \nabla\eta_n(\mathbf{r}, t)$

$$F = \int_V \left\{ m f_0(\vec{\eta}) + \frac{\kappa}{2} \sum_{i=1}^n (\nabla\eta_i)^2 \right\} dV, \quad (1)$$

where the homogeneous free energy density $f_0(\vec{\eta}) = f_0(\eta_1, \eta_2, \dots, \eta_n)$ is expressed as

$$f_0(\vec{\eta}) = \sum_{i=1}^n \left(\frac{\eta_i^4}{4} - \frac{\eta_i^2}{2} \right) + \gamma \sum_{i=1}^n \sum_{i>j} \eta_i^2 \eta_j^2 + \frac{1}{4}. \quad (2)$$

* nele.moelans@mtm.kuleuven.be

The parameters m, κ, γ are model parameters, which together define interface energy and interface width (see the following section for more details).

The governing equations for each phase field η_p are obtained based on the functional derivative of the free energy functional with respect to η_p , assuming that the phase-fields are non-conserved, i.e.

$$\frac{\partial \eta_p}{\partial t} = -L \frac{\delta F}{\delta \eta_p} = -L \left[\frac{\partial f}{\partial \eta_p} - \nabla \cdot \frac{\partial f}{\partial (\nabla \eta_p)} \right], \quad (3)$$

where L is the kinetic coefficient (also dependent on the model parameters), f is the full integrand in (1) and $\nabla \cdot \partial f / \partial (\nabla \eta_p)$ is divergence of vector field $\partial f / \partial (\nabla \eta_p)$ defined by relation

$$\frac{\partial f}{\partial (\nabla \eta_p)} = \frac{\partial f}{\partial (\partial_x \eta_p)} \mathbf{n}_x + \frac{\partial f}{\partial (\partial_y \eta_p)} \mathbf{n}_y + \frac{\partial f}{\partial (\partial_z \eta_p)} \mathbf{n}_z \quad (4)$$

with $\partial_x, \partial_y, \partial_z$ being operators for unidirectional derivatives in the corresponding directions and $\mathbf{n}_x, \mathbf{n}_y, \mathbf{n}_z$ coordinate base vectors.

A. Isotropic model

In a system with uniform grain boundary properties, the interface energy is equal for all interfaces and hence the phase-field model parameters m, κ, γ (and interface width l) are constant in the system.

Then, using expression (3), the governing equation for each phase field η_p takes the following form

$$\frac{\partial \eta_p}{\partial t} = -L \left[m \left(\eta_p^3 - \eta_p + 2\gamma \eta_p \sum_{j \neq p} \eta_j^2 \right) - \kappa \nabla^2 \eta_p \right] \quad (5)$$

The interface energy σ of the system is related to the model parameters via

$$\sigma = g(\gamma) \sqrt{m \kappa}, \quad (6)$$

where $g(\gamma)$ is a non-analytic function of parameter γ and represents integral of scaled free energy density f . The integration is taken along a straight line perpendicularly through the interface. The interface width l is expressed as

$$l = \sqrt{\frac{\kappa}{m f_{0c}(\gamma)}}, \quad (7)$$

where $f_{0c}(\gamma)$ is the value of $f_0(\eta_{i,cross}, \eta_{j,cross})$ in the points where the two phase fields η_i, η_j cross. $f_{0c}(\gamma)$ is a non-analytic function too. Values of both $g(\gamma)$ and $f_{0c}(\gamma)$ were tabulated and are available in [11].

Usually, the interface energy σ is known as material property and l is chosen for computational convenience, together with γ . Then, the parameter values are assigned from the following formulae

$$\kappa = \sigma l \frac{\sqrt{f_{0c}(\gamma)}}{g(\gamma)} \approx \frac{3}{4} \sigma l \quad (8)$$

$$m = \frac{\sigma}{l} \frac{1}{g(\gamma) \sqrt{f_{0c}(\gamma)}} \approx 6 \frac{\sigma}{l} \quad (9)$$

$$L = \frac{\mu}{l} \frac{g(\gamma)}{\sqrt{f_{0c}(\gamma)}} \approx \frac{4}{3} \frac{\mu}{l} \quad (10)$$

The symbol μ stands for interface mobility. The approximate relations above hold exactly when $\gamma = 1.5$ and are well applicable when $0.9 \leq \gamma \leq 2.65$ [19].

B. Anisotropic model and parameters assignment strategies

Two cases of interface energy anisotropy may occur, together or separately. Firstly, in the system there may be multiple interfaces with different interface energies (termed *misorientation dependence* in [19], here *pair-wise isotropy* for greater generality). Secondly, there may be an interface with inclination-dependent interface energy. Additionally, the kinetic coefficient L can be inclination dependent.

In both cases of anisotropy in interface energy, some of the model parameters m, κ, γ must become spatially dependent in order to assure correct local representation of the interface energy and width. In other words, the equations (6) and (7) must hold in every point of the anisotropic system. These two equations locally form an undetermined system of three variables, hence one of the model parameters is free and many different parameters assignment strategies are possible.

In this paper, the parameter m is always a constant, because when m was spatially varied [19], the model behavior in multijunctions was reported to be strongly affected by the interface width. Such model would be non-quantitative and thus will not be further regarded in this paper.

Three different parameters assignment strategies are considered, which differ in value of m and further in which of parameters κ, γ is constant and which varies in space to keep equation (6) valid. The three strategies are denoted: IWc (variable γ, κ so that interface width is constant [19]), IWvG (variable interface width and γ [11]) and IWvK (variable interface width and κ). Table I summarizes, which parameters are kept constant and which vary to capture the anisotropy in the different strategies. Detailed procedure of the parameters assignment and ways to control the width of the narrowest interface are described in S.I of the Supplemental Material [23]. Note that for the IWc model we propose a single-step parameters determination procedure, which is more predictable and simpler than the original iterative one [19].

The two are equivalent, though.

Below follow details about the incorporation of pair-wise isotropy and inclination-dependence in the model.

TABLE I. Characterization of the three parameter assignment strategies: the one with constant interface width (IWc), with variable interface width and all anisotropy in γ (IWvG) and with variable interface width and all anisotropy in κ (IWvK). In the latter, it is inconvenient to choose other value of γ than $\gamma = 1.5$. IW stands for interface width, other symbols have meaning as in the text.

| | IWc | IWvG | IWvK |
|--------------------|------------------|--------------|--------------|
| fixed parameters | IW, m | κ, m | γ, m |
| varying parameters | γ, κ | IW, γ | IW, κ |

1. Systems with pair-wise isotropic IE

In the system with n phase fields, there are $n(n-1)/2$ possible pair-wise interfaces, each of which may have different (mean) interface energy $\sigma_{i,j}$. The indices i, j denote interface between phase fields η_i, η_j . A set of parameters $m, \kappa_{i,j}, \gamma_{i,j}, L_{i,j}$ (all scalars) is obtained by appropriate procedure (depending on the strategy, see S.I in Supplemental Material [23]) so that the relations (6) and (7) are valid for each interface independently (equations (8)-(10) hold for each interface (i,j)). Then, these are combined together to produce the model parameter fields $\kappa(\mathbf{r}), \gamma(\mathbf{r}), L(\mathbf{r})$:

$$\kappa(\mathbf{r}) = \frac{\sum_{i=1}^n \sum_{j>i} \kappa_{i,j} \eta_i^2 \eta_j^2}{\sum_{i=1}^n \sum_{j>i} \eta_i^2 \eta_j^2} \quad (11)$$

$$\gamma(\mathbf{r}) = \frac{\sum_{i=1}^n \sum_{j>i} \gamma_{i,j} \eta_i^2 \eta_j^2}{\sum_{i=1}^n \sum_{j>i} \eta_i^2 \eta_j^2}, \quad (12)$$

$$L(\mathbf{r}) = \frac{\sum_{i=1}^n \sum_{j>i} L_{i,j} \eta_i^2 \eta_j^2}{\sum_{i=1}^n \sum_{j>i} \eta_i^2 \eta_j^2} \quad (13)$$

which stand in place of κ, γ in the functional in equation (1) and in place of L in the governing equation (3).

Notice that from Table I stems that in IWvG is $\kappa(\mathbf{r}) = \text{const}$ by definition (i.e. all the $\kappa_{i,j}$ s are equal) and similarly in IWvK $\gamma(\mathbf{r}) = \text{const} = 1.5$ (i.e. all $\gamma_{i,j}$ s are equal).

The free energy functional for IWc is then (those for IWvG and IWvK are equal, only with either $\kappa(\mathbf{r})$ or $\gamma(\mathbf{r})$ being constants, respectively):

$$F = \int_V \left\{ m f_0(\vec{\eta}) + \frac{\kappa(\mathbf{r})}{2} \sum_{i=1}^n (\nabla \eta_i)^2 \right\} dV, \quad (14)$$

$$f_0(\vec{\eta}) = \sum_{i=1}^n \left(\frac{\eta_i^4}{4} - \frac{\eta_i^2}{2} \right) + \sum_{i=1}^n \sum_{i>j} \gamma_{i,j} \eta_i^2 \eta_j^2 + \frac{1}{4}. \quad (15)$$

Both parameter fields $\kappa(\mathbf{r}), \gamma(\mathbf{r})$ are functions of phase fields $\vec{\eta}$. This dependence should produce new terms in the governing equations (from $\partial f / \partial \eta_p$ in equation (3)). However, because the denominator of $\gamma(\mathbf{r})$ cancels out in the functional, the new terms only arise from $\partial \kappa / \partial \eta_p$. The governing equations then are

$$\begin{aligned} \frac{\partial \eta_p}{\partial t} = & -L(\mathbf{r}) \left[m \left(\eta_p^3 - \eta_p + 2\eta_p \sum_{j \neq p} \gamma_{p,j} \eta_j^2 \right) \right. \\ & \left. + \frac{1}{2} \frac{\partial \kappa}{\partial \eta_p} \sum_{i=1}^n (\nabla \eta_i)^2 - \kappa(\mathbf{r}) \nabla^2 \eta_p \right] \end{aligned} \quad (16)$$

The above procedure is fully variational, nevertheless inclusion of the term proportional to $\partial \kappa / \partial \eta_p$ enables the model to reduce the total energy of the system by introduction of so called third phase contributions (also ghost or spurious phases) at diffuse interfaces. [19] That is a common problem in multi-phase field models [15], where a third phase field attains non-zero value within an interface of two other phase fields. This mathematical artefact affects triple junction angles and in general is not physically justified. Several ways of elimination or suppression of ghost phases were described in [15] and the references therein.

In this work, the ghost phases were eliminated by neglecting the term proportional to $\partial \kappa / \partial \eta_p$. However, because such model is not fully variational, the thermodynamic consistency can no longer be guaranteed in IWc and IWvK. This does not affect IWvG, because there is $\partial \kappa / \partial \eta_p = 0$ anyway. That accounts for a clear advantage of the IWvG model, as no ghost phases appear even when fully variational.

2. Systems with inclination-dependent interface energy

The orientation of an interface in 2D system is given by interface normal, inclined under the angle θ . Local value of interface energy may be a function of local interface inclination, i.e. $\sigma = \sigma(\theta)$. In Moelans' model [19], the normal at interface between η_i, η_j , denoted $\hat{\mathbf{n}}_{i,j}$, is defined as

$$\hat{\mathbf{n}}_{i,j} = \frac{\nabla \eta_i - \nabla \eta_j}{|\nabla \eta_i - \nabla \eta_j|} = \begin{bmatrix} (\hat{n}_{i,j})_x \\ (\hat{n}_{i,j})_y \end{bmatrix} \quad (17)$$

and the definite inclination of that normal

$$\theta_{i,j} = \text{atan2}[(\hat{n}_{i,j})_y, (\hat{n}_{i,j})_x], \quad (18)$$

which is the standard 2-argument arctangent function. In 2D, the inclination-dependence of interface energy can be expressed as

$$\sigma_{i,j}(\theta_{i,j}) = \sigma_{i,j}^0 h_{i,j}(\theta_{i,j}) \quad (19)$$

where $\sigma_{i,j}^0$ is a scalar and $h_{i,j}(\theta_{i,j})$ is anisotropy function. The used anisotropy function was

$$h_{i,j}(\theta_{i,j}) = 1 + \delta \cos(n \theta_{i,j}), \quad (20)$$

TABLE II. Inclination dependence of the variable parameters in the respective models. The interface energy is $\sigma_{i,j}(\theta_{i,j}) = \sigma_{i,j}^0 h_{i,j}(\theta_{i,j})$. Symbols $\kappa_{i,j}^0, \gamma_{i,j}^0$ stand for scalar values of the parameters determined from $\sigma_{i,j}^0$ (see S.I in [23]). Expressions for $\gamma_{i,j}(\theta_{i,j})$ follow the so called *weak anisotropy approximation* [19], i.e. they assume that the values of $\gamma_{i,j}(\theta_{i,j})$ do not diverge far from 1.5, so that the approximation $g^2[\gamma_{i,j}(\theta_{i,j})] \approx 16[2\gamma_{i,j}(\theta_{i,j}) - 1]/9[2\gamma_{i,j}(\theta_{i,j}) + 1]$ is applicable (see [19] for details). Second row contains expressions used in equations 23 and 24.

| model | IWc | IWvG | IWvK |
|---|--|--|--|
| variable parameter(s) | $\kappa_{i,j}(\theta_{i,j}) = \kappa_{i,j}^0 h_{i,j}(\theta_{i,j})$ $\gamma_{i,j}(\theta_{i,j}) = -\frac{\frac{9}{2}g^2(\gamma_{i,j}^0)h_{i,j}(\theta_{i,j})+1}{\frac{9}{2}g^2(\gamma_{i,j}^0)h_{i,j}(\theta_{i,j})-2}$ | $\gamma_{i,j}(\theta_{i,j}) =$ $-\frac{\frac{9}{4}[g(\gamma_{i,j}^0)h_{i,j}(\theta_{i,j})]^2+1}{\frac{9}{2}[g(\gamma_{i,j}^0)h_{i,j}(\theta_{i,j})]^2-2}$ | $\kappa_{i,j}(\theta_{i,j}) =$ $\kappa_{i,j}^0 [h_{i,j}(\theta_{i,j})]^2$ |
| $\partial\kappa_{i,j}/\partial h_{i,j}$ and $\partial\gamma_{i,j}/\partial h_{i,j}$ | $\partial\kappa_{i,j}/\partial h_{i,j} = \kappa_{i,j}^0$ $\partial\gamma_{i,j}/\partial h_{i,j} = \frac{9g^2(\gamma_{i,j}^0)}{\left[\frac{9}{2}g^2(\gamma_{i,j}^0)h_{i,j}(\theta_{i,j})-2\right]^2}$ | $\partial\gamma_{i,j}/\partial h_{i,j} =$ $\frac{18g^2(\gamma_{i,j}^0)h_{i,j}(\theta_{i,j})}{\left\{\frac{9}{2}[g(\gamma_{i,j}^0)h_{i,j}(\theta_{i,j})]^2-2\right\}^2}$ | $\partial\kappa_{i,j}/\partial h_{i,j} =$ $2\kappa_{i,j}^0 h_{i,j}(\theta_{i,j})$ |

with δ being strength of anisotropy and n the order of symmetry. Some properties of this anisotropy function and the resulting Wulff shapes are given in S.II of the Supplemental Material [23].

The inclination dependence of $\sigma_{i,j}$ implies that some of the model parameters $\gamma_{i,j}, \kappa_{i,j}$ must be taken inclination-dependent too. Depending on the model used (IWc, IWvG or IWvK), the local validity of equation (6) is achieved using different inclination dependence of the variable parameters (see Table II for details).

Because the inclination-dependent $\kappa_{i,j}, \gamma_{i,j}$ are functions of components of gradients $\nabla\eta_i, \nabla\eta_j$, the divergence term in the functional derivative (equation (3)) produces additional driving force terms. In the general case with multiple inclination-dependent interfaces, the divergence term equals

$$\begin{aligned}
\nabla \cdot \frac{\partial f}{\partial(\nabla\eta_p)} &= 2m\eta_p \nabla\eta_p \cdot \left[\sum_{j \neq p} \eta_j^2 \frac{\partial\gamma_{p,j}}{\partial(\nabla\eta_p)} \right] \\
&+ 2m\eta_p^2 \sum_{j \neq p} \left[\eta_j \nabla\eta_j \cdot \frac{\partial\gamma_{p,j}}{\partial(\nabla\eta_p)} \right] \\
&+ m\eta_p^2 \sum_{j \neq p} \eta_j^2 \left[\nabla \cdot \frac{\partial\gamma_{p,j}}{\partial(\nabla\eta_p)} \right] \\
&+ \frac{1}{2} \left[\nabla \cdot \frac{\partial\kappa}{\partial(\nabla\eta_p)} \right] \sum_{i=1}^n (\nabla\eta_i)^2 \\
&+ \frac{1}{2} \frac{\partial\kappa}{\partial(\nabla\eta_p)} \cdot \left[\nabla \sum_{i=1}^n (\nabla\eta_i)^2 \right] \\
&+ \nabla\kappa(\mathbf{r}) \cdot \nabla\eta_p + \kappa(\mathbf{r}) \nabla^2\eta_p.
\end{aligned} \tag{21}$$

The vector field $\partial\kappa/\partial(\nabla\eta_p)$ is

$$\frac{\partial\kappa}{\partial(\nabla\eta_p)} = \frac{\sum_{j \neq p} \left(\frac{\partial\kappa_{p,j}}{\partial(\nabla\eta_p)} \right) \eta_p^2 \eta_j^2}{\sum_{k=1}^n \sum_{l>k} \eta_k^2 \eta_l^2} \tag{22}$$

where the sum in the nominator goes through all pairwise interfaces of $\eta_p(\mathbf{r})$. The vector fields $\partial\kappa_{p,j}/\partial(\nabla\eta_p)$

are expressed

$$\frac{\partial\kappa_{p,j}}{\partial(\nabla\eta_p)} = \frac{1}{|\nabla\eta_i - \nabla\eta_j|} \frac{\partial\kappa_{p,j}}{\partial h_{p,j}} \frac{\partial h_{p,j}}{\partial\theta_{p,j}} \begin{bmatrix} -(\hat{n}_{i,j})_y \\ (\hat{n}_{i,j})_x \end{bmatrix}. \tag{23}$$

Note, that the above vector field is nonzero only in IWc and IWvK models at the interfaces ($p-j$) with inclination-dependent IE. Likewise, the below vector field is nonzero only in IWc and IWvG

$$\frac{\partial\gamma_{p,j}}{\partial(\nabla\eta_p)} = \frac{1}{|\nabla\eta_i - \nabla\eta_j|} \frac{\partial\gamma_{p,j}}{\partial h_{p,j}} \frac{\partial h_{p,j}}{\partial\theta_{p,j}} \begin{bmatrix} -(\hat{n}_{i,j})_y \\ (\hat{n}_{i,j})_x \end{bmatrix}. \tag{24}$$

The multipliers $\partial\kappa_{p,j}/\partial h_{p,j}$ and $\partial\gamma_{p,j}/\partial h_{p,j}$ differ in individual models and are also provided in Table II. The term $\partial h_{p,j}/\partial\theta_{p,j}$ is defined by the inclination-dependence at the interface ($p-j$).

The governing equation then is

$$\frac{\partial\eta_p}{\partial t} = -L(\mathbf{r}) \left[m \left(\eta_p^3 - \eta_p + 2\eta_p \sum_{j \neq p} \gamma_{p,j}(\theta_{p,j}) \eta_j^2 \right) - \nabla \cdot \frac{\partial f}{\partial(\nabla\eta_p)} \right]. \tag{25}$$

Note, that the term proportional to $\partial\kappa/\partial\eta_p$ was neglected here.

In models with variable interface width (IWvG, IWvK), at the interfaces with inclination-dependent interface energy, the interface width is a function of the inclination, i.e. $l_{i,j} = l_{i,j}(\theta_{i,j})$. Because the kinetic coefficient $L_{i,j}$ is inversely proportional to the interface width $l_{i,j}$ (see equation (10)), the kinetic coefficient is inclination-dependent as well (even for *constant* grain boundary mobility $\mu_{i,j}$). The inclination dependence of $L_{i,j}(\theta_{i,j})$ due to interface width variation is in the IWvG model

$$L_{i,j}(\theta_{i,j}) = L_{i,j} h_{i,j}(\theta_{i,j}) \tag{26}$$

and in the IWvK model

$$L_{i,j}(\theta_{i,j}) = L_{i,j} / h_{i,j}(\theta_{i,j}), \tag{27}$$

where $h_{i,j}(\theta_{i,j})$ is the anisotropy function in interface energy (19).

The equations (26),(27) were derived from an alternative expression for the kinetic coefficient $L_{i,j}$,

$$L_{i,j} = \frac{\mu_{i,j} \sigma_{i,j}(\theta_{i,j})}{\kappa_{i,j}(\theta_{i,j})}, \quad (28)$$

where the inclination dependencies of the right-hand side were expressed correspondingly to the model (see Table II for $\kappa_{i,j}(\theta_{i,j})$).

Due to varying number of driving force terms in the three parameter assignment strategies, the governing equations are different in each and hence it is justified to call them different models.

3. Systems with inclination-dependent mobility

Let the interface $(i-j)$ have isotropic interface energy and inclination-dependent grain boundary mobility with anisotropy function $h_{i,j}^\mu(\theta_{i,j})$, i.e. $\mu_{i,j} = \mu_{i,j}(\theta_{i,j}) = \mu_{i,j}^0 h_{i,j}^\mu(\theta_{i,j})$. From equation (10) we can see that the kinetic coefficient must have the same anisotropy, i.e. $L_{i,j}(\theta_{i,j}) = L_{i,j}^0 h_{i,j}^\mu(\theta_{i,j})$, where $L_{i,j}^0 = \mu_{i,j}^0 g(\gamma_{i,j})/l_{i,j} f_{0c}(\gamma_{i,j})$.

If the interface energy is inclination-dependent as well and a model with variable interface width is used (either IWvG or IWvK), the inclination dependence in $L_{i,j}(\theta_{i,j})$ due to the interface width variation must be included similarly like in (26) and (27). The physical inclination-dependence is independent from the one due to interface width variation, implying the following expression for IWvG model

$$L_{i,j}(\theta_{i,j}) = L_{i,j}^0 h_{i,j}(\theta_{i,j}) h_{i,j}^\mu(\theta_{i,j}) \quad (29)$$

and for the IWvK model analogically

$$L_{i,j}(\theta_{i,j}) = L_{i,j}^0 \frac{h_{i,j}^\mu(\theta_{i,j})}{h_{i,j}(\theta_{i,j})}, \quad (30)$$

where $h_{i,j}(\theta_{i,j})$ is the interface energy anisotropy function.

III. NUMERICAL IMPLEMENTATION

All models were implemented in a single MATLAB function, where the governing equations were solved by centered finite differences of second order, explicit Euler time stepping and boundary conditions implemented using ghost nodes. The minimal code to run the simulations is available in the dataset [24].

During the parameters assignment in models with variable interface width (IWvG, IWvK), there was assured control over the minimal interface width, i.e. that there would be no interface narrower than the user-specified

one. That is to prevent unphysical behavior of the interface due to too small grid resolution. Different strategies had to be adopted in IWvK and IWvG, respectively. They are described in Supplemental Material [23] together with other best practices in parameters determination for the respective models. MATLAB functions which were used for parameters determination were also included in the dataset [24].

The Supplemental Material [23] further contains several practical details regarding the implementation such as time step determination as function of the anisotropy, the used finite-difference stencil and the driving force localization on the interface for solver stability.

In the simulations with inclination-dependent interface energy, the vector field $\partial\kappa/\partial(\nabla\eta_p)$ was computed as in equations (22) and (23), the fields $\partial\gamma_{p,j}/\partial(\nabla\eta_p)$ as in equation (24) and their divergences (see equation (21)) were computed numerically (by centered differences), as well as the gradient $\nabla\kappa(\mathbf{r})$. All the above terms were computed in the IWc model, whereas in the models with variable interface width some of them could be omitted (as explained in section II B 2).

When the anisotropy in inclination-dependent interface energy was strong (i.e. $\delta > 1/(n^2 - 1)$ or $\Omega > 1$), the anisotropy function had to be regularized as described in [25] in order to avoid ill-posedness of the governing equations for interfaces with missing inclination.

IV. METHODOLOGY

Four different simulation experiments were performed: shrinking circles, triple junction angles, shrinking Wulff shape and kinetically compensated anisotropic curvature-driven circle shrinkage. The initial-state geometries and basic information is in Figure 1. Except for the shrinking circles simulation, a parametric study was carried out in every experiment in order to validate the model behavior. Table III summarizes the variable parameters in every experiment.

Each of the experiments was simulated using all the three model modifications (IWc, IWvG and IWvK) successively and the results were quantitatively compared.

In order to distinguish the behavior of the model from the artefacts of numeric discretization, the above described series of simulations was re-run for several numeric settings. Throughout the paper, these large series are called 'runs'.

In total, there were four runs, the basic settings of which are summarized in Table IV. The difference between the runs were: a) the minimal set interface width l_{min} and b) the number of points in the interface. The runs are denoted base run, IW/2, 14IWpts and 1000IW. The base run had rather coarse grid and 7 points in the interface, which should in general be reliable yet not very computationally heavy settings. The minimal interface width was $l_{min} = 1$ nm. In the run IW/2 the interface width was halved ($l_{min} = 0.5$ nm) and the number of

TABLE III. Overview of the simulations carried out in every simulation experiment. Note that these were carried out in every model modification (i.e. IWc, IWvG and IWvK) and simulation run (see Table IV). Number of simulations in every experiment is provided in the column Count. See text for more details.

| Experiment | Varied par. | Values | Count |
|------------------------|--------------------------------|---|-------|
| shrinking circles | $(\sigma_{top}, \sigma_{bot})$ | $(0.1, 0.3) \text{ J/m}^2$ | 1 |
| triple junction | $\sigma_1/\sigma_2 (-)$ | 0.13, 0.2, 0.3, 0.4, 0.5, 0.6, 0.7, 0.8, 0.9, 1.0 1.1, 1.2, 1.3, 1.4, 1.5, 1.6, 1.7, 1.8, 1.9, 2.0 | 20 |
| Wulff shape | $\Omega (-)$ | 0.2, 0.4, 0.6, 0.8, 1.0, 2.3, 3.6, 4.9, 6.2, 7.5 | 10 |
| Kin.comp.aniso. circle | $\Omega (-)$ | 0.1, 0.3, 0.5, 0.7, 0.9 | 5 |

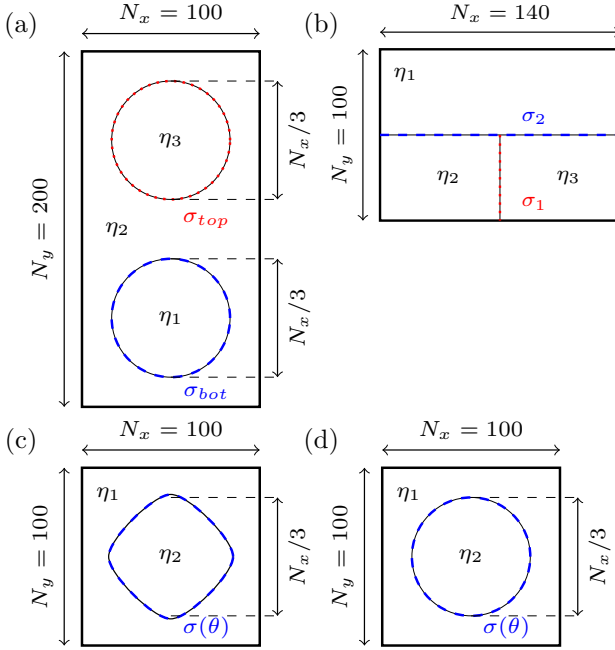


FIG. 1. Initial conditions in the different numeric experiments with indicated interface energies. In a) shrinking circles, $\sigma_2 = 0.3\sigma_1$, b) triple junctions angle, c) Wulff shape simulation and d) kinetically compensated anisotropic curvature-driven circle shrinkage. Grid dimensions correspond to the base run and 1000IW run (see text for details). All interfaces have equal mobilities.

points in the interface was 7 again. In the 14IWpts run, the interface width was as in the base run but the points in the interface were doubled (to be 14). Physical dimensions of the simulated domain were equal in the described runs but the grid spacing was halved in IW/2 and 14IWpts runs. In the last 1000IW run, the grid was equal as in the base run, but the physical dimensions were scaled by a factor of 1000, meaning the minimal interface width $l_{min} = 1 \mu\text{m}$. This is the practical settings for the actual grain growth simulations. The latter run validated that the meso-scale behavior of the model is equal to that one at the nanometer scale.

In the simulation experiments, position of the interface in the respective geometry was compared to the expected shape. Depending on the parameters assignment strat-

TABLE IV. Numeric settings of different simulation runs (for each simulation experiment and model). l_{min} is the minimal interface width. N_x and N_y are grid dimensions in the base run as shown in Figure 1

| | base run | IW/2 | 14IWpts | 1000IW |
|---------------------|------------------|--------------------|--------------------|------------------|
| grid dimensions | $N_x \times N_y$ | $2N_x \times 2N_y$ | $2N_x \times 2N_y$ | $N_x \times N_y$ |
| l_{min} (nm) | 1 | 0.5 | 1 | 1000 |
| points in l_{min} | 7 | 7 | 14 | 7 |

egy, the phase field profiles may not be symmetric about the point 0.5 in Moelans' model (as apparent in Figure 2). For this reason, it was considered that the position of the interface $i-j$ was in points $\mathbf{r} = (x, y)$ of the domain, where $\eta_i(\mathbf{r}) = \eta_j(\mathbf{r})$, i.e. where the two profiles crossed. This way the contours were always well defined and could be quantitatively compared to appropriate analytical models even for Wulff shape simulations, where the profile shape varies along the interface.

The below subsections in detail describe the simulation experiments and the respective results processing.

A. Shrinking circles

Because the phase fields are non-conserved and the boundaries move towards the center of curvature, in 2D simulation a circle in a matrix must shrink. In this case, the rate of shrinkage dA/dt is constant in time and the interface velocity is constant along the circle perimeter (hence the circle does not deform). The shrinkage rate can be expressed analytically as [26]

$$\frac{dA}{dt} = -2\pi\sigma\mu. \quad (31)$$

Figure 1a sketches the initial condition, in which each circle had different interface energy, with for the bottom circle having $\sigma_{bot} = 0.3 \text{ J/m}^2$, and for the top circle $\sigma_{top} = 0.3\sigma_{bot}$. Because the interface mobilities were equal, the bottom circle shrunk faster due to its higher interface energy. This experiment demonstrates the difference in profiles of the individual model modifications.

B. Triple junction angles

The initial geometry was like in Figure 1b with periodic left and right boundaries, and Neumann boundary conditions on the top and bottom ones. The individual interfaces are isotropic but have different interface energies. The initially straight interface segments (1-2) and (1-3) with grain boundary energy σ_2 turn into circular arcs, which then move towards the center of curvature, i.e. downwards. The two grains η_2 and η_3 will shrink and in the steady state the angle α between the arcs (see Figure 4a) in the triple junction is described by Young's law [27] (section 3.3.3):

$$\alpha = 2\arccos(0.5\sigma_1/\sigma_2). \quad (32)$$

The ratio σ_1/σ_2 was varied in the parametric study to validate the model (see Table III). It was always $\sigma_1 = 0.3 \text{ J/m}^2$ and σ_2 was computed from the ratio.

The phase field contours of interfaces (1-2) and (1-3) were analyzed by two methods in order to determine the triple junction angle α . First, the points on both the arcs nearest to the triple junction were fitted by a straight line (indicated by red segments in Figure 4a) and second, the remaining arc points were fitted by a circular arc (see green segments in Figure 4a). Simple geometric construction allows to determine the angle α from the fitted parameters in the latter case [26] as

$$\alpha = 2\arccos(x/R), \quad (33)$$

where R is the fitted circle arc radius and x is the horizontal distance from the triple junction (see the scheme in Figure 4a). Width of the interval in which the arcs were fitted by straight lines (width of pink rectangles in Figure 4a) was set to width of the interface (2-3) (i.e. half of the width on each side).

Accuracy of the lines fitting is affected especially by the width of the above interval and that of the circle arc fitting is mostly affected by the simulated arc shape.

C. Wulff shape

The Neumann boundary conditions were applied to all boundaries in a system with initial condition like in Figure 1c. The simulations were carried out for different strengths of anisotropy Ω . In order to shorten the simulation time to reach the steady state, the initial condition for each run was a Wulff shape of a weaker strength of anisotropy (instead of a circle). The goodness of match of the phase field contour to the analytic Wulff shape was represented by the mean sum of squared residuals in radius

$$\Sigma\Delta^2 = \sum_i^N (r_i^{PF} - r_i^{anal})^2/N, \quad (34)$$

where r_i^{PF}, r_i^{anal} are radii in i -th point on the phase-field contour and on the analytic Wulff shape, respectively. The Wulff shape \mathbf{w} in 2D is a curve, which can be parametrized by the interface normal angle θ , i.e. $\mathbf{w}(\theta) = [w_x(\theta), w_y(\theta)]^T$, giving [25, 28, 29]

$$w_x(\theta) = R_W[h(\theta)\cos(\theta) - h'(\theta)\sin(\theta)] \quad (35)$$

$$w_y(\theta) = R_W[h(\theta)\sin(\theta) + h'(\theta)\cos(\theta)], \quad (36)$$

where R_W is the radius of the Wulff shape (arbitrary) and $h(\theta), h'(\theta)$ the anisotropy function and its derivative, respectively. The sum in (34) goes through all N contour points. The closer is $\Sigma\Delta^2$ to zero, the better the match. With $h(\theta) = 1 + \delta \cos(n\theta)$, the minimal distance R_{min} between the Wulff shape center and the contour can be related to R_W as

$$R_{min} = R_W(1 - \delta), \quad (37)$$

which holds for arbitrarily strong anisotropy because the minimal-radius point normal is always inclined under a non-missing angle. This formula was used to find the radius R_W to compare the phase-field simulation contours to the analytic Wulff shape. Detailed procedure of matching the phase field contours to the analytic shapes is in S.IV of the Supplemental Material [23].

In the presented results, the $\Sigma\Delta^2$ was computed from 500 polar-angle-equidistant points on the contour in Wulff shape simulation.

To validate also the kinetics of the shrinking Wulff shapes, an analytic expression for their shrinkage rate was derived in S.III of Supplemental Material [23]. Measurement of area/volume occupied by a grain/phase is trivial in phase field method, hence the rate of its change (i.e. the shrinkage rate) can be easily used for validation. The derivation in [23] delivers the expression

$$\frac{dA_W}{dt} = 2\pi\mu\sigma_0 \frac{C_W(\Omega, n)}{1 - \delta} \quad (38)$$

where $C_W(\Omega, n) = A_W/A_{circle}$ is an anisotropic factor relating the area of a Wulff shape and a circle of equal radius. The shrinkage rate results are presented in two ways: a) the end-of-simulation shrinkage rate, which is the shrinkage rate in the last time step of the simulation, and b) the shrinkage rate evolution in simulation time. Because the analytic shrinkage rate is a constant, the observed one (evolving in simulation time) should converge to the predicted value and remain constant.

In this paper, only fourfold symmetry was assumed.

D. Kinetically compensated anisotropic circle shrinkage

This simulation experiment validates the inclination-dependence of the kinetic coefficient in combination with inclination-dependent interface energy. Specifically, the anisotropy of kinetic coefficient was chosen such that it

compensated the anisotropic driving force so that the resulting interface motion was isotropic.

Again, the normalized strength of anisotropy Ω was varied to validate the model.

Normal velocity v_n of a curvature-driven interface with inclination-dependent interface energy is

$$v_n(\theta) = \frac{\mu}{\varrho} \sigma_0 [f(\theta) + f''(\theta)], \quad (39)$$

where μ is interface mobility, ϱ is local radius of curvature and $\sigma_0 [f(\theta) + f''(\theta)]$ is the interface stiffness. With $f(\theta) = 1 + \delta \cos(n\theta)$ the inclination-dependent factor in (39) is $[f(\theta) + f''(\theta)] = 1 - \delta(n^2 - 1) \cos(n\theta) = 1 - \Omega \cos(n\theta)$.

When the interface mobility is set anisotropic as

$$\mu(\theta) = \frac{\mu_0}{1 - \Omega \cos(n\theta)}, \quad (40)$$

the resulting interface normal velocity v_n does not depend on interface inclination θ anymore, i.e. it is isotropic. The below presented simulations were all carried out with $\Omega < 1$, because the kinetic coefficient as in equation (40) is then positive for all interface inclinations.

The ratio of maximal to minimal interface velocity due to the anisotropic interface energy is $(1 + \Omega)/(1 - \Omega)$, which indicates rather strong kinetic anisotropy when Ω is close to 1. E.g. with $\Omega = 0.9$ the ratio of maximal to minimal interface velocity is 19 (assuming constant ϱ for all inclinations, which holds for a circle). Note that the corresponding ratio of maximal to minimal interface energy is only 1.0664 (with four-fold symmetry).

The initial condition for the simulation experiment was as in Figure 1d, i.e. a two-phase-field system of a circular grain in a matrix. The expected shrinkage rate is that from equation (31) and the analytic contour is circle. The normalized sum of squared differences $\Sigma \Delta^2$ between the phase field contour and the circle was used to assess the match as in the Wulff shape simulations (taking 300 angle-equidistant contour points).

V. RESULTS

A. Shrinking circles

Figure 2 shows radial sections of the phase fields representing the top and bottom circle with the different model modifications in the base run (in 2a) and IW/2 run (in 2b). Apparently, in the IWvG model modification, the interface with the smallest interface energy (σ_{top}) exhibits the larger interface width, while in the IWvK the reverse is observed (the interface is wider for the higher interface energy σ_{bot}). Notice in Figure 2a that in IWvK the phase field values in the bottom circle center are smaller than 1 due to the interface width being too large in comparison to

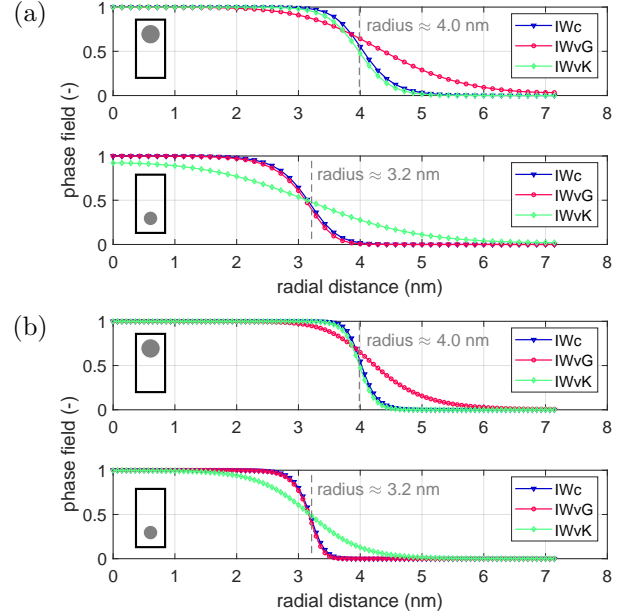


FIG. 2. Demonstration of 1D phase field interface profiles obtained for the different model modifications from the simulations starting from the initial structure depicted in Fig. 1a. In (a) the phase field profiles as observed in the base run, in (b) as in the IW/2 run. In the top graphs of both (a) and (b), the top-circle profile is shown, in the bottom graphs there is the bottom circle (see the insets in the respective graphs).

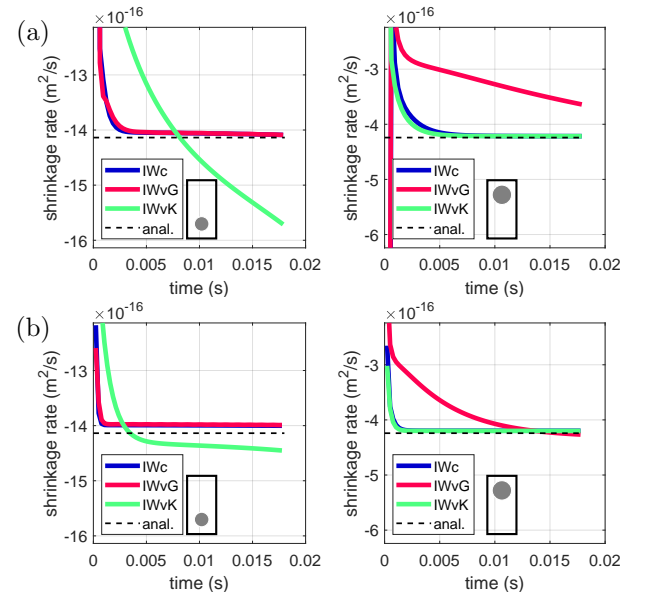


FIG. 3. Time evolution of shrinkage rates of the two grains compared for the different model modifications from the simulations starting from the initial structure depicted in Fig. 1a for (a) base run and (b) IW/2 run. Graphs on the left show the evolution for the bottom circle and those on the right for the top circle (as indicated in the insets).

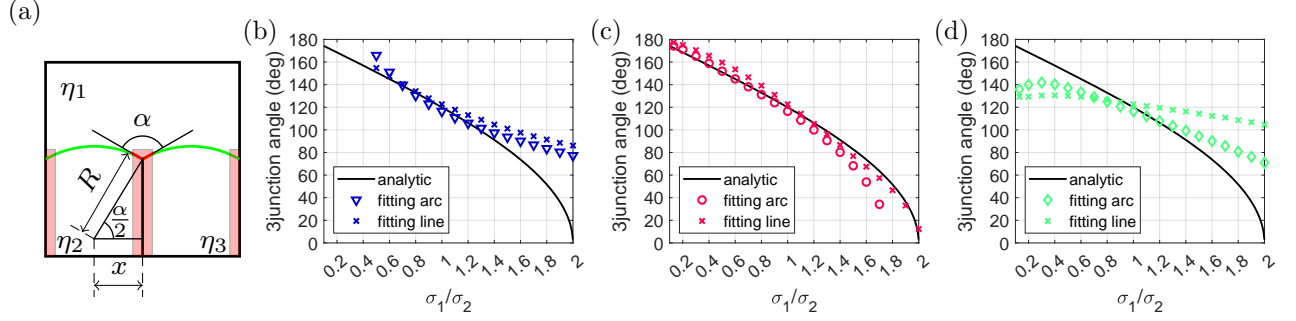


FIG. 4. Triple junction angles. In a) the two methods for angles determination are illustrated (points fitted by straight lines in red and those fitted by circular arc in green). Subfigures b)-d) show the simulation results for different models, these being: in b) IWc, in c) IWvG and in d) IWvK. The hollow symbols correspond to the the angles determined by arc fitting and crosses to the lines fitting.

the circle radius. Specifically, the wider interface in IWvK has width $l_{wide} = l_{min}\sigma_{top}/\sigma_{bot} = 3.333l_{min}$ (see S.I in Supplemental Material [23]). In IWvG it is $l_{wide} = 3.3l_{min}$.

Time evolution of the shrinkage rate for both circles and the different models in base run is shown in Figure 3a and the one for the run IW/2 in Figure 3b. It is expected that the shrinkage rate converges to a value given by equation (31). In both models with variable interface width (IWvG and IWvK), the kinetics was strongly affected in the wide-interface circles. This was significantly improved by reduction of the interface width by half in the IW/2 run. In the narrow-interface circles (and for IWc), the kinetics matched well the analytic model.

The IWvG model apparently develops the wider equilibrium profile significantly longer than IWc or IWvK.

No significant effect on results was observed in runs 14IWpts and 1000IW, which all together implies that a) the kinetics was negatively affected where the interface width was comparable to the size of the simulated feature, b) 7 points in the interface are enough to provide quantitative results, and c) the model results are unaffected by scaling of the domain by a factor 1000, i.e. it is quantitative. Point a) implies that with stronger anisotropies rather finer simulation grids are needed so that even the widest interfaces are reasonably narrow.

B. Equilibrium triple junction angles

Figures 4b-4d show the simulation results from the triple junction simulations as function of σ_1/σ_2 . Neither of IWc or IWvK models show good agreement to Young's law when deviating farther from an isotropic system (which has ratio $\sigma_1/\sigma_2 = 1$). The model IWvG, on the other hand, always shows very good agreement in at least one of the fitting methods along the whole range of probed ratios of interface energies. With σ_1/σ_2 closer to 2 in IWvG modification, the grains shape was slightly

elongated in the vertical direction, resulting in too small radius of the fitted arcs to cross in the triple junction. The angles could not be determined this way then and the linear fit is more reliable.

For the ratios approximately $\sigma_1/\sigma_2 \leq 0.45$ the IWc model behaves non-physically. The triple junction was observed to move in the opposite than expected direction (i.e. upwards, as if the triple junction angle was larger then 180°). The overall shape of contours was not as in Figure 4a because the green arcs curved in the other way. In IWvK this behavior was not observed, but the Young's law is not followed. Qualitative explanation is that the IWc and IWvK models are not fully variational. No significant change was observed in the results of the triple junction angles in runs IW/2, 14IWpts or 1000IW when compared to the base run. Quality of the results is thus not improved when more points in the interface than 7 are used. Also it implies, that the model behavior (for all parameters assignment strategies) is not affected by reducing the interface-width-to-feature ratio or the interface width scaling. The latter confirms that the model is quantitative.

C. Wulff shapes

The Figures 5a-5f visually compare the Wulff shapes obtained from simulation by the different models (in base run) to the analytic ones. The simulation time was long enough to reach the steady state shape (confirmed by inspection of time evolution of the mean sum of squared residuals $\Sigma\Delta^2$). As can be seen, the overall match is very good in all the three models, although rather round contour near the corners in strong-anisotropy Wulff shapes are observed (this is more apparent in Figure 6b, which shows detail of the contours near a corner for $\Omega = 7.5$). That was expected, as no special finite difference scheme was used near corners (in [25] a one-sided finite difference scheme was proposed to avoid corners rounding).

Figure 6a, shows the match to Wulff shape as function of normalized strength of anisotropy Ω in the base run.

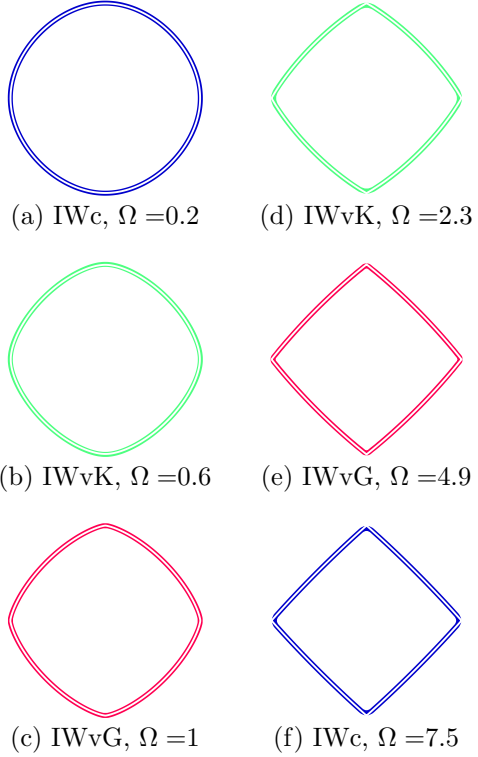


FIG. 5. Demonstration of the simulated Wulff shapes for strengths of anisotropy Ω with the different models (base run). The white line is the analytic Wulff shape and the colored ones are the extracted phase field contours.

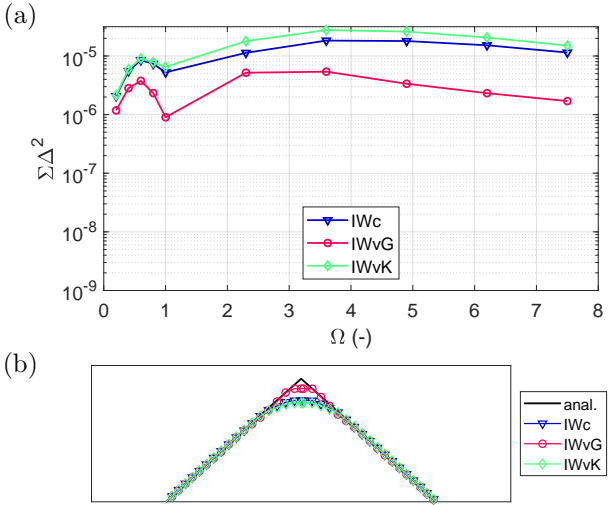


FIG. 6. In (a) the match to Wulff shape for the model modifications in the base run as function of normalized strength of anisotropy Ω . In (b) a detail of the phase field contours near the Wulff shape corner for simulation with $\Omega = 7.5$.

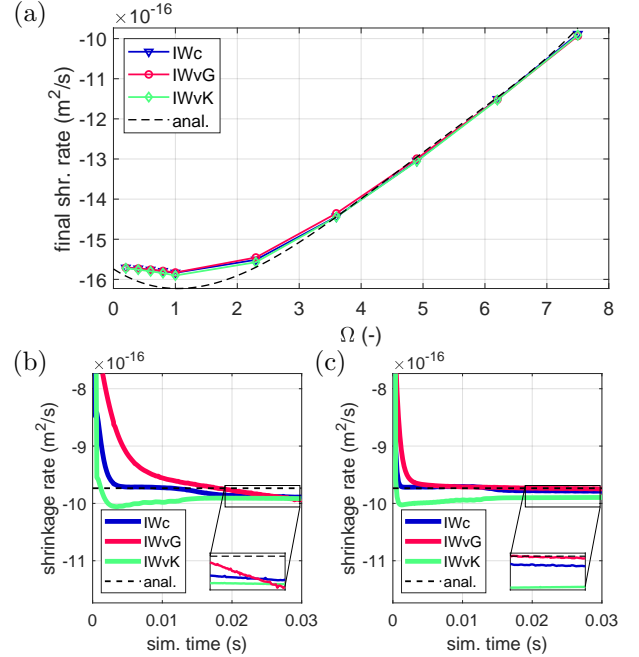


FIG. 7. Wulff shape shrinkage rate results. In (a) the end-of-simulation shrinkage rate in the base run as function of normalized strength of anisotropy Ω , in (b) and (c) there is time evolution of shrinkage rate for $\Omega = 7.5$ in the base and IW/2 runs, respectively.

As can be seen, the IWvG model outperformed the other two. That is because it was able to resolve the corners the best (see Figure 6b). However, when the interface width was halved in the IW/2 run, all the models performed nearly equally well because with smaller interface width the rounding near the corners was reduced. Interestingly, the IWvG model performed comparably in the IW/2 and base runs, which is in contrast to IWc and IWvK, which improved markedly with narrower interface width. The best results in match to Wulff shape were obtained in the 14IWpts run with IWvG model. IWc and IWvK models performed comparably in the 14IWpts and IW/2 runs.

The end-of-simulation shrinkage rates of the Wulff shapes as function of strength of anisotropy are in Figure 7a for the base run. At first sight, all the models perform comparably well, following the analytical prediction. The Figures 7b and 7c show the time evolution of shrinkage rate with $\Omega = 7.5$ in the base and IW/2 runs, respectively. It can be seen that despite the end-of-simulation shrinkage rates being near the prediction, in the base run, the shrinkage rate of IWvG model did not converge to the analytic prediction (see the inset of Figure 7b, where the IWvG curve clearly declines). In the IW/2 run the IWvG model did converge close to the analytic shrinkage rate (see also the inset of Figure 7c) and all the end-of-simulation values are a little closer than in the base run. Note that in the IWvG model the lowest-energy interface has the widest interface width and that

the cornered Wulff shape contains only interface orientations with lower energy. For this reason it required narrower interface width to reach constant shrinkage rate.

In addition to the four simulation runs discussed so far, the Wulff shapes simulations were re-run also with 4 and 5 points in the interface. The match to Wulff shape was worse than with 7 or 14 points, but the shapes were resolved qualitatively well regardless. The shrinkage rates were smaller than expected though, due to grid pinning. Seven points in the interface were thus confirmed as a reasonable value for practical simulations.

No significant effect of interface width scaling in the run 1000IW was found.

D. Kinetically compensated anisotropic circle shrinkage

The quantified match to the circle and the end-of-simulation shrinkage rate as functions of strength of anisotropy Ω are in Figures 8a and 8b, respectively (results of the base run showed). All models and runs retained the initial circle well or up to excellent geometrical match. Nevertheless, the IWvG model gave the best results, except for the strongest anisotropy, where the IWvK model was better. Only minor improvement in the match was achieved in the IW/2 run when compared to the base run. As with Wulff shapes simulations, the best match was obtained in the 14IWpts run, which also exhibited the best end-of-simulation shrinkage rates (for all the three models).

The end-of-simulation shrinkage rates in Figure 8b show slightly rising trend with Ω for IWc and IWvG models. The values of IWvK model were not affected by the rising anisotropy and were constant. Apparently, the symmetric profiles of IWvK model provide an advantage for preserving the expected kinetics in simulations with strong kinetic inclination dependence.

Time evolution of shrinkage rate for the strongest considered anisotropy (i.e. $\Omega = 0.9$) in Figures 8c and 8d (base and 14IWpts runs, respectively), shows that in both runs the lines slightly diverge (this being applicable to all Ω s). The convergence was better in IW/2 run, but the end-of-simulation shrinkage rates were worse than in the 14IWpts run.

Apparently, optimal results would be obtained here with more points than 7 in the interface and with smaller interface-width-to-circle ratio than in the base run and 14IWpts runs. However, as noted earlier, the kinetic anisotropy is very strong in the case of $\Omega = 0.9$. For weaker anisotropy the discussed effects are less pronounced and there is little difference in the shrinkage rates among the models.

There was no significant difference between the results of base and 1000IW runs.

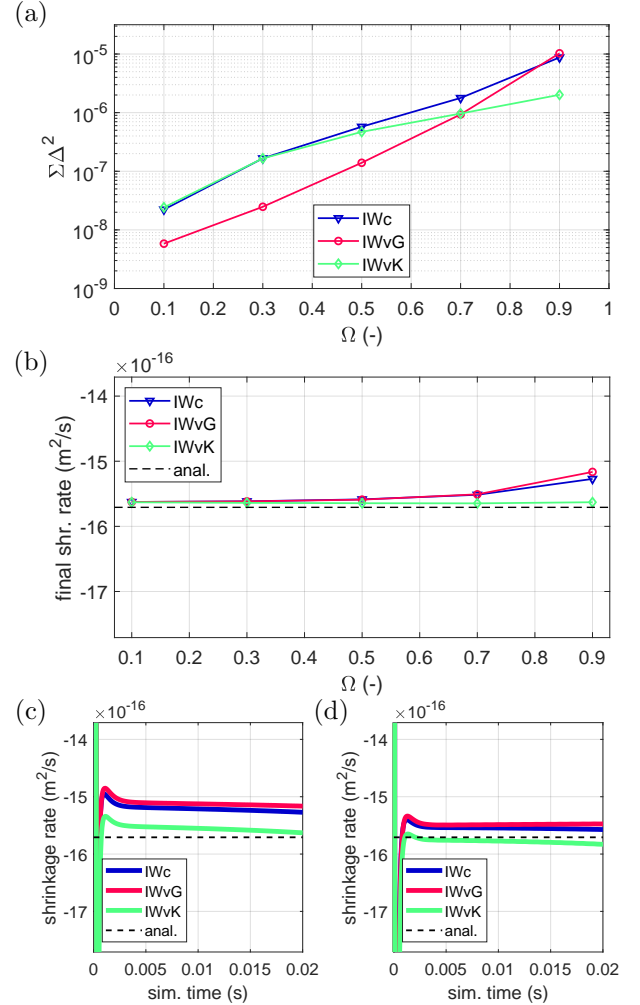


FIG. 8. Results for kinetically compensated anisotropic shrinkage. In (a) the match to circle for the base run, in (b) the end-of-simulation shrinkage rate for 14IWpts run, in (c) and (d) the shrinkage rate time evolution in simulation with $\Omega = 0.9$ in the base run and 14IWpts runs, respectively.

VI. CONCLUSIONS

This paper presented a thorough comparison of three modifications of a grain growth model with anisotropic grain boundary properties, with emphasis on the inclination-dependent interface energy. The modifications differed in the way the model parameters were assigned to individual interfaces in order to represent the same physical input. Different parameters assignment strategy resulted in different shapes of phase field profiles at the interface, which in turn affected the model behavior, especially in the modifications with variable interface width, i.e. IWvG and IWvK.

Four different simulation experiments were carried out, in three of which the defining parameters were varied in order to validate and compare the model modifications. All simulations were re-run with various numeric settings

of the interface in order to isolate the model behavior from numerical artefacts due to discretization.

The difference between the model modifications was largest in the triple junction angles. Otherwise the different behavior was mostly due to the differently varying interface width for stronger anisotropies in the models with variable interface width. However, all the models modifications were able to reproduce the anisotropic curvature driving force, as evidenced by good match to Wulff shapes and, given enough narrow interface width, their shrinkage rates.

Nevertheless, of the compared models, generally it is advisable to use the model modification IWvG (with variable interface width and all anisotropy in γ). It was shown to be superior to the IWc and IWvK modifications, the most importantly in the triple junction angles of pair-wise isotropic interfaces. There, IWc and

IWvK are only applicable to rather mild anisotropies, where there is little difference between the models anyway. Additionally, the IWvG reached the highest accuracy in match to Wulff shapes even without refining the interface width. However, the variable interface width remains the largest limitation of the model, implying especially the need of finer simulation grids to assure correct kinetics.

The parameters assignment procedures described in S.I of Suplemental Material [23] assured that no interface was narrower than a user-defined value, which was important for predictable behavior of the model.

No results were significantly affected by the interface width scaling. Also, it was confirmed that 7 points in the interface were sufficient for retaining the expected kinetics in most cases, unless the inclination dependence of the kinetic coefficient was very strong.

[1] G. S. Rohrer, Grain boundary energy anisotropy: A review, *Journal of Materials Science* **46**, 5881 (2011).

[2] D. L. Olmsted, S. M. Foiles, and E. A. Holm, Survey of computed grain boundary properties in face-centered cubic metals: I. Grain boundary energy, *Acta Materialia* **57**, 3694 (2009).

[3] V. V. Bulatov, B. W. Reed, and M. Kumar, Grain boundary energy function for fcc metals, *Acta Materialia* **65**, 161 (2014).

[4] E. Miyoshi, T. Takaki, M. Ohno, Y. Shibuta, S. Sakane, T. Shimokawabe, and T. Aoki, Correlation between three-dimensional and cross-sectional characteristics of ideal grain growth: large-scale phase-field simulation study, *Journal of Materials Science* **53**, 15165 (2018).

[5] J. Gao, M. Wei, L. Zhang, Y. Du, Z. Liu, and B. Huang, Effect of Different Initial Structures on the Simulation of Microstructure Evolution During Normal Grain Growth via Phase-Field Modeling, *Metallurgical and Materials Transactions A: Physical Metallurgy and Materials Science* **49**, 6442 (2018).

[6] H. Mao, B. Li, and Y. Du, A comprehensive analysis of three-dimensional normal grain growth of pure iron via multi-phase field simulation, *Journal of Mining and Metallurgy, Section B: Metallurgy* **57**, 105 (2021).

[7] S. G. Kim, D. I. Kim, W. T. Kim, and Y. B. Park, Computer simulations of two-dimensional and three-dimensional ideal grain growth, *Physical Review E - Statistical, Nonlinear, and Soft Matter Physics* **74**, 1 (2006).

[8] V. Yadav and N. Moelans, Investigation on the existence of a ‘Hillert regime’ in normal grain growth, *Scripta Materialia* **142**, 148 (2018).

[9] Y. H. Song, M. T. Wang, J. Ni, J. F. Jin, and Y. P. Zong, Effect of grain boundary energy anisotropy on grain growth in ZK60 alloy using a 3D phase-field modeling, *Chinese Physics B* **29**, 10.1088/1674-1056/abad1f (2020).

[10] V. Yadav, L. Vanherpe, and N. Moelans, Effect of volume fractions on microstructure evolution in isotropic volume-conserved two-phase alloys: A phase-field study, *Computational Materials Science* **125**, 297 (2016).

[11] H. Ravash, J. Vleugels, and N. Moelans, Three-dimensional phase-field simulation of microstructural evolution in three-phase materials with different interfacial energies and different diffusivities, *Journal of Materials Science* **52**, 13852 (2017).

[12] N. Moelans, F. Spaepen, and P. Wollants, Grain growth in thin films with a fibre texture studied by phase-field simulations and mean field modelling, *Philosophical Magazine* **90**, 501 (2010).

[13] K. Chang and N. Moelans, Effect of grain boundary energy anisotropy on highly textured grain structures studied by phase-field simulations, *Acta Materialia* **64**, 443 (2014).

[14] H. Garcke, B. Stoth, and B. Nestler, Anisotropy in multiphase systems: a phase field approach, *Interfaces and Free Boundaries* **1**, 175 (1999).

[15] G. I. Tóth, T. Pusztai, and L. Gránásy, Consistent multiphase-field theory for interface driven multidomain dynamics, *Physical Review B - Condensed Matter and Materials Physics* **92**, 1 (2015), arXiv:1508.04311.

[16] H. Salama, J. Kundin, O. Shchyglo, V. Mohles, K. Marquardt, and I. Steinbach, Role of inclination dependence of grain boundary energy on the microstructure evolution during grain growth, *Acta Materialia* **188**, 641 (2020).

[17] A. Kazaryan, Y. Wang, and S. Dregia, Generalized phase-field model for computer simulation of grain growth in anisotropic systems, *Physical Review B - Condensed Matter and Materials Physics* **61**, 14275 (2000), arXiv:9912044 [cond-mat].

[18] F. Wendler, C. Mennерich, and B. Nestler, A phase-field model for polycrystalline thin film growth, *Journal of Crystal Growth* **327**, 189 (2011).

[19] N. Moelans, B. Blanpain, and P. Wollants, Quantitative analysis of grain boundary properties in a generalized phase field model for grain growth in anisotropic systems, *Physical Review B - Condensed Matter and Materials Physics* **78**, 10.1103/PhysRevB.78.024113 (2008).

[20] E. Miyoshi, T. Takaki, M. Ohno, and Y. Shibuta, Accuracy evaluation of phase-field models for grain growth simulation with anisotropic grain boundary properties, *ISIJ International* **60**, 160 (2020).

[21] N. Moelans, A quantitative and thermodynamically con-

sistent phase-field interpolation function for multi-phase systems, *Acta Materialia* **59**, 1077 (2011).

[22] N. Moelans, F. Spaepen, and P. Wollants, Grain growth in thin films with a fibre texture studied by phase-field simulations and mean field modelling, *Philosophical Magazine* **90**, 501 (2010).

[23] M. Minar and N. Moelans, See Supplemental material at xxx for the best practices in parameters determination in Moelans' model and for further details on the implementation., *Phys.Rev.Mat.* (2022).

[24] M. Minar, Three strategies of parameters assignment in multi phase field model of grain growth with anisotropic grain boundary properties, Mendeley Data, v1 10.17632/5wr3ky9pp.1 (2022).

[25] J. Eggleston, G. McFadden, and P. Voorhees, A phase-field model for highly anisotropic interfacial energy, *Physica D: Nonlinear Phenomena* **150**, 91 (2001).

[26] N. Moelans, F. Wendler, and B. Nestler, Comparative study of two phase-field models for grain growth, *Computational Materials Science* **46**, 479 (2009).

[27] D. A. Porter, K. E. Easterling, and K. E. Easterling, *Phase Transformations in Metals and Alloys (Revised Reprint)*, 3rd ed. (CRC Press, 2009).

[28] W. K. Burton, N. Cabrera, and F. C. Frank, The Growth of Crystals and the Equilibrium Structure of their Surfaces, *Philosophical Transactions of the Royal Society A: Mathematical, Physical and Engineering Sciences* **243**, 299 (1951).

[29] R. Kobayashi and Y. Giga, On anisotropy and curvature effects for growing Crystals, *Japan Journal of Industrial and Applied Mathematics* **18**, 207 (2001).

Supplemental Material for

Comparison of three different strategies to introduce anisotropic interface properties in a multi-phase-field model

Martin Minar and Nele Moelans*
KU Leuven, Department of Materials Engineering
(Dated: January 5, 2022)

S.I. MODEL PARAMETERS DETERMINATION - BEST PRACTICES

The best practices in parameters determination described in this section were implemented in MATLAB functions, which were published in dataset [1], distributed under GPLv3 license.

A. Polynomial expressions for determination of γ

Interface energy and width are non-analytic functions of the parameter γ (equations (6) and (7) in the main text). In models IWc and IWvG with non-uniform interface energy, γ varies in space and depends on physical input (local interface energy σ) and chosen interface width. Assuming that κ, m and σ are known, $g(\gamma)$ is computed using equation (6) and must be inverted in order to obtain γ . For numeric convenience, functions $g^2 \rightarrow 1/\gamma$ and $1/\gamma \rightarrow f_{0,c}$ were fitted by polynomials using the tabulated values from [2]. The same approach was taken in [3]. Note that in one of the following subsections an alternative algorithm for determination of parameters in IWc is proposed.

The values of $f_{0,c}(\gamma), g(\gamma)$ were tabulated and published in [2] in the range $0.52 \leq \gamma \leq 40$. However, the polynomials used in both [2, 3] did not describe the functions along the whole tabulated range. For inconvenient input, that resulted in a loss of control over the interface properties (even negative values of γ were obtained).

To improve the parameters determination, the functions $g^2 \rightarrow 1/\gamma$ and $1/\gamma \rightarrow f_{0,c}$ were fitted again so that all γ values from the interval $0.52 \leq \gamma \leq 40$ were reliably available. The new polynomials show good agreement along the given interval and their coefficients are listed in Table S.1.

TABLE S.1: Coefficients of the new polynomials used in the parameters determination algorithm (IWc and IWvG models). Based on fitting of the numeric values given in [2]. The polynomial of order N $p_N(x)$ is defined here together with its coefficients as $p_N(x) = \sum_{i=0}^N a_i x^{N-i}$. See text for details of use in the respective models.

| | order | a_0 | a_1 | a_2 | a_3 | a_4 | a_5 | a_6 |
|--|-------|-----------|----------|----------|-----------|----------|-----------|----------|
| $g^2 \rightarrow \frac{1}{\gamma}$ | 6 | -5.73008 | 18.8615 | -23.0557 | 7.47952 | 8.33568 | -8.01224 | 2.00013 |
| $\frac{1}{\gamma} \rightarrow \sqrt{f_{0,c}}$ | 5 | -0.072966 | 0.35784 | -0.68325 | 0.63578 | -0.48566 | 0.53703 | |
| $g\sqrt{f_{0,c}} \rightarrow \frac{1}{\gamma}$ | 6 | 103.397 | -165.393 | 105.3469 | -44.55661 | 24.7348 | -11.25718 | 1.999642 |

B. IWvG

This parameters determination algorithm [2] requires input of initializing interface energy σ_{init} , and width l_{init} which are assigned to interface with value $\gamma = 1.5$. There, the analytic relations between the model parameters are valid and the (constant) parameters κ, m can be computed:

$$\kappa = \frac{3}{4} \sigma_{init} l_{init} \quad , \quad m = 6 \frac{\sigma_{init}}{l_{init}}. \quad (\text{S.1})$$

These are then used in equation (6) with individual interface energies $\sigma_{i,j}$ to determine $g^2(\gamma_{i,j})$ and further $\gamma_{i,j}$ (using the first polynomial from Table S.1).

* nele.moelans@mtm.kuleuven.be

However, because the said polynomial was only fitted in the interval $0.52 \leq \gamma \leq 40$ (values tabulated in [2]), it is important to choose the value of σ_{init} such, that none of the interface energies $\sigma_{i,j}$ should be described by $\gamma_{i,j}$ out of the interval. From equation (6) with substituted \sqrt{km} from S.1 we show that the values do not leave the above interval when σ_{init} complies with the following two inequalities

$$\frac{\sigma_{max}}{g(40)} \sqrt{\frac{2}{9}} \leq \sigma_{init} \leq \frac{\sigma_{min}}{g(0.52)} \sqrt{\frac{2}{9}}, \quad (\text{S.2})$$

where $\sigma_{min}, \sigma_{max}$ are minimal and maximal interface energy present in the system. Additionally, in order to fulfill these conditions, it must be satisfied that

$$\frac{\sigma_{min}}{\sigma_{max}} \geq \frac{g(0.52)}{g(40)} = \frac{0.1}{0.76} = 0.129, \quad (\text{S.3})$$

which sets the maximal anisotropy in interface energy for which all $\gamma_{i,j}$ s may be determined in IWvG based on the values tabulated in [2].

Control over the width of the narrowest interface (with user-defined width l_{min}) is obtained when the parameters are determined in two steps as follows:

1. values of κ, m are calculated from equations (S.1) using appropriate σ_{init} together with l_{min}
2. values of κ, m are recalculated from equations (S.1) with the same σ_{init} and interface width $l_{calib} = l_{min} \sqrt{8f_{0,c}(\gamma_{min})}$, where γ_{min} corresponds to the lowest value of all the $\gamma_{i,j}$ obtained in the previous step, i.e. to the interface with the largest interface energy σ_{max} .

After the second step, the interface with maximal interface energy will have the width l_{min} and all the other interfaces will have it equal or larger.

The other interface widths can be expressed

$$l_{i,j} = \frac{\sigma_{i,j}}{m} \frac{1}{g(\gamma_{i,j}) \sqrt{f_{0,c}(\gamma_{i,j})}} \quad (\text{S.4})$$

C. IWc

The iterative parameters determining procedure assuring the constant interface width is described in [3]. The procedure requires initializing value of interface energy σ_{init} , which has decisive role for the parameters values. For inconvenient choice of σ_{init} , some of the parameters $\gamma_{i,j}$ may get out of range of applicability of the polynomials in Table S.1. Systematic investigation revealed that the value $\sigma_{init} = (\sigma_{max} + \sigma_{min})/2$ prevents occurrence of such effects for anisotropies $\sigma_{min}/\sigma_{max} \geq 0.03$.

Here we propose a simplified, yet equivalent single-step procedure. We assume constant interface width l and an initializing interface energy σ_{init} , for which $\gamma = 1.5$ and thus the analytic relations between the model parameters hold. As in the original iterative algorithm, the barrier height is computed

$$m = 6 \frac{\sigma_{init}}{l}. \quad (\text{S.5})$$

Then, the gradient energy coefficient $\kappa_{i,j}$ can be expressed from both equations (7) and (8), hence we can write

$$\kappa_{i,j} = f_{0,c}(\gamma_{i,j}) ml^2 = \sigma_{i,j} l \frac{\sqrt{f_{0,c}(\gamma_{i,j})}}{g(\gamma_{i,j})}, \quad (\text{S.6})$$

from where we obtain

$$g(\gamma_{i,j}) \sqrt{f_{0,c}(\gamma_{i,j})} = \frac{\sigma_{i,j}}{ml} = \frac{\sigma_{i,j}}{6\sigma_{init}}. \quad (\text{S.7})$$

In the last equation, m was substituted from (S.5). We denote $G(\gamma_{i,j}) = g(\gamma_{i,j}) \sqrt{f_{0,c}(\gamma_{i,j})}$. This function $\gamma \rightarrow G$ can be evaluated from the data tabulated in [2] and its inverse function $G \rightarrow \frac{1}{\gamma}$ was fitted by 6-th order polynomial producing the coefficients in the last row of Table S.1. Apparently, evaluation of this polynomial in points $\sigma_{i,j}/6\sigma_{init}$

produces the searched $1/\gamma_{i,j}$. The gradient energy coefficients are then best computed as in S.6, where m was substituted from S.5:

$$\kappa_{i,j} = 6f_{0,c}(\gamma_{i,j})\sigma_{init}l. \quad (\text{S.8})$$

Here, the fitted polynomial $\frac{1}{\gamma} \rightarrow \sqrt{f_{0,c}}$ is used to obtain the values of $f_{0,c}(\gamma_{i,j})$.

Similarly like in IWcG model, there are conditions limiting suitable values of σ_{init}

$$\frac{\sigma_{max}}{6G(40)} \leq \sigma_{init} \leq \frac{\sigma_{min}}{6G(0.52)}, \quad (\text{S.9})$$

where $G(0.52) \approx 0.0069$, $G(40) \approx 0.4065$. Also must be satisfied

$$\frac{\sigma_{min}}{\sigma_{max}} \geq \frac{G(0.52)}{G(40)} = 0.017. \quad (\text{S.10})$$

The main advantage of the proposed algorithm is that no iterations are needed for parameters determination. In the original algorithm the number of iteration steps is uncertain (tens of repetitions are not exceptional though) and sometimes the results may not converge due to reasons tedious to debug. Obtaining each parameter in a single step thus provides better control over the process and simplifies the implementation. Moreover, the permissible values of σ_{init} and the maximal anisotropy $\sigma_{min}/\sigma_{max}$ are clearly defined.

Also, it should be noted that when σ_{init} is chosen close to the upper limit in the inequality S.9, the determined $\gamma_{i,j}$ s are rather closer to value 0.52 (corresponding to long-tailed interfaces). When σ_{init} is near the bottom limit, the values of γ_{max} are close to the value 40 and γ_{min} are much larger than in the previous case. Near the limiting anisotropy $\sigma_{min}/\sigma_{max} \approx 0.017$, the values always are $\gamma_{max} \approx 40$ and $\gamma_{min} \approx 0.52$. It is especially near the limits of admissible σ_{init} , where the original iterative parameters assignment strategy is not always reliable when compared to the proposed one.

D. IWvK

When $\gamma = \text{const} = 1.5$, the analytic relations between the model parameters hold (i.e. equations (8)-(10)). Then, the minimal interface width l_{min} is controlled when

$$m = 6 \frac{\sigma_{min}}{l_{min}} \quad (\text{S.11})$$

and

$$\kappa_{i,j} = \frac{9}{2} \frac{\sigma_{i,j}^2}{m}. \quad (\text{S.12})$$

Interface width of an interface $i-j$ can then be computed as

$$l_{i,j} = 6 \frac{\sigma_{i,j}}{m}. \quad (\text{S.13})$$

S.II. PROPERTIES OF THE USED ANISOTROPY FUNCTION

Let $f(\theta)$ be a smooth anisotropy function in 2D (see e.g. [4] for more details). The Wulff shape \mathbf{w} in 2D is a curve minimizing the interface energy of a crystal with constant area. It can be parameterized by the interface normal angle θ , i.e. $\mathbf{w}(\theta) = [w_x(\theta), w_y(\theta)]^T$, giving [4–6]

$$w_x(\theta) = R_W [f(\theta) \cos(\theta) - f'(\theta) \sin(\theta)] \quad (\text{S.14})$$

$$w_y(\theta) = R_W [f(\theta) \sin(\theta) + f'(\theta) \cos(\theta)], \quad (\text{S.15})$$

where R_W is the radius of the Wulff shape (arbitrary). The radius of curvature $\varrho(\theta)$ of this Wulff shape is locally

$$\varrho(\theta) = R_W [f''(\theta) + f(\theta)], \quad (\text{S.16})$$

which may technically get negative for some θ . Because that does not have any geometric interpretation, the Wulff shape does not contain such oriented segments and the angles θ_m fulfilling $\varrho(\theta_m) \leq 0$ are called missing or forbidden. In the following, we assume the anisotropy function

$$f(\theta) = 1 + \delta \cos(n\theta) \quad (\text{S.17})$$

with strength of anisotropy $0 \leq \delta < 1$ and n an order of symmetry (integer). The interface energy is $\sigma = \sigma_0 f(\theta)$. In this case, the missing angles occur for sufficiently strong anisotropy, i.e. when

$$\delta \geq \frac{1}{n^2 - 1}, \quad (\text{S.18})$$

and span over an interval around every maximum of anisotropy function $f(\theta)$. The stronger the anisotropy, the wider the interval of missing angles. Within $-\frac{\pi}{n} \geq \theta \leq \frac{\pi}{n}$, the border points of that interval are found by solving [6]

$$\frac{d}{d\theta} \frac{\cos(\theta)}{f(\theta)} = 0. \quad (\text{S.19})$$

As the authors are unaware of analytic solution to this equation, it was solved numerically. The other ($n-1$) segments on the Wulff shape are periodic, hence all the missing angles can be obtained by rotation of the above one by multiples of $2\pi/n$.

The strong-anisotropy Wulff shape is not smooth, it contains corners (i.e. jumps in local normal orientation). When plotting such Wulff shape, the missing angles θ_m must be excluded from the θ s parameterizing $\mathbf{w}(\theta)$, otherwise "ears" behind the corners are plotted as well.

Equation (S.18) can be used to define normalized strength of anisotropy $\Omega = \delta(n^2 - 1)$, which straightforwardly distinguishes between weak anisotropy $\Omega < 1$ (smooth Wulff shape) and strong anisotropy $\Omega \geq 1$ (the cornered one).

For a given radius R_W , the area of a Wulff shape A_W differs from the area of a circle $A = \pi R_W^2$ by the anisotropy-dependent factor $C_W(\Omega, n) = A_W/A$. For weak anisotropy $\Omega < 1$ there is an analytic expression

$$C_W = 1 - \frac{\Omega^2}{n^2 - 1}, \quad (\text{S.20})$$

but there is none for strong anisotropy $\Omega > 1$. The factor $C_W(\Omega, n)$ was obtained numerically for $n = 4$ in the range $0 \leq \Omega \leq 7.5$ (the Wulff shape was plotted, its area numerically computed and divided by πR^2). There, the Ω -dependence was fitted very well by a polynomial of 4-th order $C_W(\Omega, 4) = \sum_{i=0}^4 a_i \Omega^{N-i}$ with $a_0 = -0.00032, a_1 = 0.00639, a_2 = -0.04219, a_3 = 0.00034, a_4 = 1.00000$.

S.III. SHRINKAGE RATE OF A WULFF SHAPE

The normal velocity of anisotropic curvature-driven interface in 2D is [7]

$$v_n(\theta, t) = -\frac{\mu}{\varrho(\theta, t)} \sigma_0 [f''(\theta) + f(\theta)] \quad (\text{S.21})$$

where μ is the interface mobility and $\sigma_0 [f''(\theta) + f(\theta)]$ is interface stiffness. When it is the Wulff shape shrinking, the radius of curvature $\varrho(\theta, t)$ can be expressed as in equation (S.16) and the inclination-dependent part of the interface stiffness is cancelled out. The normal velocity is then constant along the perimeter

$$v_n(t) = -\frac{\mu \sigma_0}{R_W(t)}. \quad (\text{S.22})$$

The sign is such that the interface moves towards the center of curvature.

Because the area of a Wulff shape is $A_W = \pi R_W^2 C_W(\Omega, n)$, the shrinkage rate of a Wulff shape is

$$\begin{aligned} \frac{dA_W}{dt} &= \frac{d}{dt} [\pi R_W^2(t) C_W(\Omega, n)] \\ &= 2\pi C_W(\Omega, n) R_W(t) \frac{dR_W}{dt}. \end{aligned} \quad (\text{S.23})$$

TABLE S.2: Parameters from equation (S.27) describing anisotropic dependence of the Courant number C in simulations with inclination-dependent interface energy and strong anisotropy $\Omega > 1$.

| | IWc | IWvG | IWvK |
|---|------|------|------|
| a | 1.38 | 1.43 | 0.98 |
| b | 1.95 | 1.91 | 2.35 |

Because the normal velocity is constant along the perimeter, the point R_{min} from equation (37) moves also by $v_n(t)$. Importantly, the normal of interface in R_{min} is aligned with the radial direction of the polar coordinates, hence we can write $v_n = dR_{min}/dt$. From equation (37) then must be

$$\frac{dR_W}{dt} = \frac{1}{1-\delta} \frac{dR_{min}}{dt} = \frac{1}{1-\delta} v_n(t), \quad (\text{S.24})$$

which together with S.22 implies in S.23

$$\frac{dA_W}{dt} = 2\pi\mu\sigma_0 \frac{C_W(\Omega, n)}{1-\delta} \quad (\text{S.25})$$

Taylor and Cahn [8] proved that the shrinkage rate for the equilibrium shape must be a constant, which is met by the final expression.

S.IV. GOODNESS OF MATCH OF PHASE FIELD CONTOURS TO ANALYTIC WULFF SHAPES

In order to quantify the match of phase field contours to the analytic Wulff shapes (computed by (35),(36) and expressed in polar coordinates), the following procedure was developed. First, the contour where the two phase fields crossed was located and its centroid (geometric center) was found. Then the origin of the cartesian coordinates was shifted to the centroid so that the contour points could be expressed in polar coordinates. From equation (37), the radius of the phase-field Wulff shape was obtained and used to scale it to unit radius. The phase-field contour was interpolated in equidistant polar angles and an analytic Wulff shape (of unit radius) was interpolated in the same polar angles so that the two could be compared.

S.V. ADDITIONAL REMARKS ON NUMERIC IMPLEMENTATION

In finite difference method, the ratio of the time step to the grid spacing determines the numeric stability of the simulation. Specifically, the so-called Courant number C must be $0 < C < 0.5$, where in this model

$$C = \min[\kappa(\mathbf{r})L]\Delta t/(\Delta x)^2. \quad (\text{S.26})$$

In practice, the time step was computed using equation (S.26) assuming the value of $C \leq 0.3$. For stronger anisotropies C had to be reduced farther. When $0.129 \leq \sigma_{min}/\sigma_{max} \leq 0.2$, the value $C = 0.12$ was used, when $0.2 < \sigma_{min}/\sigma_{max} \leq 0.3$, $C = 0.17$ and for $\sigma_{min}/\sigma_{max} > 0.3$ the used Courant number was $C = 0.3$. The latter value of Courant number was also applied in simulations with inclination-dependent interface energy and smooth Wulff shapes ($\Omega \leq 1$). For cornered Wulff shapes ($\Omega > 1$), the following dependence was obtained from visual inspection of the interface normal inclination field $\theta(\mathbf{r})$ defined in equation (18) ($\theta(\mathbf{r})$ was sensitive to the numeric instabilities) during the simulation

$$C(\Omega) = \frac{1}{a\Omega + b}. \quad (\text{S.27})$$

The Table S.2 contains the values of a, b in the respective model modifications.

The following 9-point stencil was used for computation of the laplacian in grid point (k, l)

$$\begin{aligned} (\nabla^2 \eta)_{k,l} = & \frac{1}{6h^2} [4(\eta_{k-1,l} + \eta_{k+1,l}\eta_{k,l-1} + \eta_{k,l+1}) \\ & + \eta_{k+1,l+1} + \eta_{k-1,l-1} + \eta_{k-1,l+1} + \eta_{k+1,l-1} \\ & - 20\eta_{k,l}]. \end{aligned} \quad (\text{S.28})$$

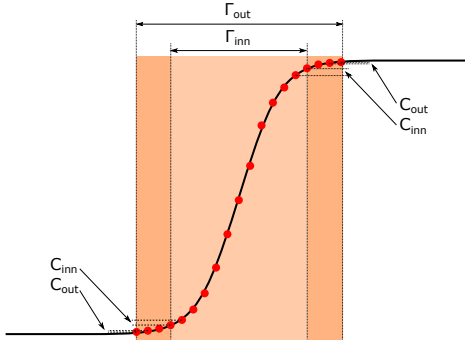


FIG. S.1: Illustration of the near-interface regions $\Gamma_{out}, \Gamma_{inn}$, defined by absolute values of difference in phase fields between neighbouring points.

When the interface energy is inclination-dependent, it can be seen in equations (23), (24) of the main text that some driving force terms are proportional to $1/|\nabla\eta_i - \nabla\eta_j|$. In fact, some are even proportional to $1/|\nabla\eta_i - \nabla\eta_j|^3$ when worked out analytically. Far enough from the interface, the magnitude $|\nabla\eta_i - \nabla\eta_j|$ inevitably gets smaller than the numeric resolution, which causes severe numeric instabilities due to locally very large driving forces. For this reason, all the driving force terms from equation (21) were only computed in a region close enough to the interface. Two such regions $\Gamma_{out}, \Gamma_{inn}$ (outer and inner) were selected based on local value of $|\nabla\eta_i - \nabla\eta_j|$ (see Figure S.1). The region Γ_{inn} was a subset of Γ_{out} . The interface inclination field $\theta_{i,j}$ was computed in Γ_{out} , where $|\nabla\eta_i - \nabla\eta_j|^3(\Delta x)^3 > C_{out}^3$ and the driving force terms $\nabla \cdot \partial f/\partial(\nabla\eta_p)$ were computed in region Γ_{inn} where $|\nabla\eta_i - \nabla\eta_j|^3(\Delta x)^3 > C_{inn}^3$. The constants $C_{out} = 10^{-6}$ and $C_{inn} = 0.005$ have the meaning of minimal local change in value of phase field which is acceptable to the respective near-interface region (this is exactly true for $\gamma = 1.5$ and approximate otherwise). Note, that the driving force from homogeneous free energy density (i.e. $\partial f/\partial\eta_p$) and the laplacian term $\kappa(\mathbf{r})\nabla^2\eta_p$ were computed and applied in the whole simulation domain.

In the Wulff shape simulations, the accuracy of match to the analytical shape with IWvG phase field contour turned out to be sensitive to alignment of the shape within the numerical grid. For strong anisotropies $\Omega > 1$, when the corner laid exactly on some grid line, the IWvG contours were slightly deformed, making the model perform seemingly worse than IWc and IWvK (which were not affected by this). This problem was solved by shifting the center of the initial shape by half a pixel in both x and y direction. No corner than laid on any grid line and that solved the problem. Rotating the Wulff shape relative to the grid had similar effect. All the results in the main text were simulated with the shifted initial shape. This is not likely to play significant role in grain growth simulations as the corner motion along grid line is very unlikely with arbitrary grain structure and local grain orientation.

[1] M. Minar, Three strategies of parameters assignment in multi phase field model of grain growth with anisotropic grain boundary properties, Mendeley Data, v1 10.17632/5wrv3ky9pp.1 (2022).

[2] H. Ravash, J. Vleugels, and N. Moelans, Three-dimensional phase-field simulation of microstructural evolution in three-phase materials with different interfacial energies and different diffusivities, *Journal of Materials Science* **52**, 13852 (2017).

[3] N. Moelans, B. Blanpain, and P. Wollants, Quantitative analysis of grain boundary properties in a generalized phase field model for grain growth in anisotropic systems, *Physical Review B - Condensed Matter and Materials Physics* **78**, 10.1103/PhysRevB.78.024113 (2008).

[4] R. Kobayashi and Y. Giga, On anisotropy and curvature effects for growing Crystals, *Japan Journal of Industrial and Applied Mathematics* **18**, 207 (2001).

[5] W. K. Burton, N. Cabrera, and F. C. Frank, The Growth of Crystals and the Equilibrium Structure of their Surfaces, *Philosophical Transactions of the Royal Society A: Mathematical, Physical and Engineering Sciences* **243**, 299 (1951).

[6] J. Eggleston, G. McFadden, and P. Voorhees, A phase-field model for highly anisotropic interfacial energy, *Physica D: Nonlinear Phenomena* **150**, 91 (2001).

[7] F. Abdeljawad, S. M. Foiles, A. P. Moore, A. R. Hinkle, C. M. Barr, N. M. Heckman, K. Hattar, and B. L. Boyce, The role of the interface stiffness tensor on grain boundary dynamics, *Acta Materialia* **158**, 440 (2018).

[8] J. E. Taylor and J. W. Cahn, Diffuse interfaces with sharp corners and facets: Phase field models with strongly anisotropic surfaces, *Physica D: Nonlinear Phenomena* **112**, 381 (1998).